A robust method for the automatic location of the optic disc and the fovea in fundus images

Roberto Romero-Oraá , María García , Javier Oraá-Pérez , María I. López , Roberto Hornero

PII: S0169-2607(20)31432-2
DOI: https://doi.org/10.1016/j.cmpb.2020.105599
Reference: COMM 105599

To appear in: *Computer Methods and Programs in Biomedicine*

Received date: 19 December 2019
Accepted date: 1 June 2020

Please cite this article as: Roberto Romero-Oraá , María García , Javier Oraá-Pérez , María I. López , Roberto Hornero , A robust method for the automatic location of the optic disc and the fovea in fundus images, *Computer Methods and Programs in Biomedicine* (2020), doi: https://doi.org/10.1016/j.cmpb.2020.105599

HIGHLIGHTS

- **Novel saliency maps representing the location of the optic disc and the fovea**
- **Novel method for retinal background extraction based on region growing**
- **Robust results using four different databases**

A robust method for the automatic location of the optic disc and the fovea in fundus images

Roberto Romero-Oraá[a,b,*], María García[a,b], Javier Oraá-Pérez[a], María I. López[a,b,c,d] and Roberto Hornero[a,b,e]

[a] Biomedical Engineering Group, Universidad de Valladolid, Valladolid, 47011, Spain. (roberto.romero@gib.tel.uva.es, maria.garcia@tel.uva.es, javier.oraa@gib.tel.uva.es, roberto.hornero@tel.uva.es).

[b] Centro de Investigación Biomédica en Red de Bioingeniería, Biomateriales y Nanomedicina (CIBER-BBN), Spain

[c] Department of Ophthalmology, Hospital Clínico Universitario de Valladolid, Valladolid, 47003, Spain.

[d] Instituto Universitario de Oftalmobiología Aplicada (IOBA), Universidad de Valladolid, Valladolid, 47011, Spain (maribel@ioba.med.uva.es).

[e] Instituto de Investigación en Matemáticas (IMUVA), Universidad de Valladolid, Valladolid, 47011, Spain.

* Corresponding author: **Roberto Romero-Oraá**

Biomedical Engineering Group, E.T.S. Ingenieros de Telecomunicación, Universidad de Valladolid, Campus Miguel Delibes, Paseo Belén 15, 47011 – Valladolid, Spain.

Tel. +34 983 423000 ext. 5589

E-mail address: roberto.romero@gib.tel.uva.es

URL: www.gib.tel.uva.es

Abstract-

Background and objective. The location of the optic disc (OD) and the fovea is usually crucial in automatic screening systems for diabetic retinopathy. Previous methods aimed at their location often fail when these structures do not have the standard appearance. The purpose of this work is to propose novel, robust methods for the automatic detection of the OD and the fovea.

Methods. The proposed method comprises a preprocessing stage, a method for retinal background extraction, a vasculature segmentation phase and the computation of various novel saliency maps. The main novelty of this work is the combination of the proposed saliency maps, which represent the spatial relationships between some structures of the retina and the visual appearance of the OD and fovea. Another contribution is the method to extract the retinal background, based on region-growing.

Results: The proposed methods were evaluated over a proprietary database and three public databases: DRIVE, DiaretDB1 and Messidor. For the OD, we achieved 100% accuracy for all databases except Messidor (99.50%). As for the fovea location, we also reached 100% accuracy for all databases except Messidor (99.67%).

Conclusions: Our results suggest that the proposed methods are robust and effective to automatically detect the OD and the fovea. This way, they can be useful in automatic screening systems for diabetic retinopathy as well as other retinal diseases.

Keywords- diabetic retinopathy, fundus image, computer-assisted diagnostic systems, optic disc, fovea.

1. INTRODUCTION

Diabetic retinopathy (DR) is the most common and serious complication of diabetes mellitus (DM). With the increasing incidence of DM, DR has become a leading cause of blindness globally [1,2]. Early detection for adequate treatment is the only way to prevent blindness and visual loss. Unfortunately, no external symptoms appear in the early stages of DR [1]. Therefore, regular DR screening based on fundus images analysis is necessary [1–3]. However, the manual analysis of these images requires a lot of time, effort and costs, being non-viable for large populations [4]. Hence, computer-aided diagnosis systems (CADS) are necessary to assist ophthalmologists.

The optic disc (OD) and the fovea are the most important anatomical landmarks in fundus images, together with the vasculature. The detection of these structures is usually crucial in CADS [5]. The OD is the exit point of the optic nerve and appears a bright yellow disc in fundus images. It is also the area from which the vasculature emerges [5]. Parts of the OD look similar to some DR-related lesions, such as exudates, which hinders the differentiation among them [5]. Additionally, the OD center is a reference point for locating other retinal structures, like the fovea [6]. Consequently, the OD detection is highly recommended before further processing [7]. The macula is the area of the fundus containing maximum density of cones, the color receptors of the visual system. It appears darker than the rest of the retinal background [8]. The fovea is the central region of the macula and responsible for sharp central vision. For this reason, lesions near this area are especially relevant. Therefore, the location of the fovea also plays an important role in CADS [5].

A number of different approaches can be found in literature for detecting the OD. Exclusively locating the OD center allows estimating the OD by means of a circumference, which is enough to differentiate OD and lesions [9,10]. Originally, Sinthayothin et al. [11] proposed using the pixel intensity variation. Other authors applied template matching [9] or morphological filtering and watershed transformation [12]. Multiple studies rely on the vasculature to locate the OD [5,13,14]. Additionally, a *k*-nearest neighbor (*k*-NN) classifier was included in [5]. Later, Lu

[15] used a circular transformation while Qureshi et al. [16] proposed a combination of techniques comprising pyramidal decomposition, edge detection and entropy filter. A spatial weighted graph was defined in [7] and an illumination correction method was studied by Hsiao et al. [17]. Other studies were based on swarm techniques, including ant colony [18], firefly algorithms [19] and different swarm intelligence algorithms [20]. Deep learning has also been used in some recent studies [6].

The detection of the fovea has also received attention. Some studies considered the anatomical position of the fovea relative to the OD and the vasculature [8,21,22]. Additionally, some of them applied mathematical morphology [8,22]. Li and Chutatape [23] modeled the main vessel arcades using a parabolic curve. Then, they considered the low intensity pixels to locate the fovea. Niemeijer et al. [24] used a cost function based on both global and local features. Feature extraction techniques were also applied in [21] to find the center of the fovea. Other authors combined several algorithms by applying special geometric rules in order to improve the performance of the individual algorithms [16]. The use of Fast Radial Symmetry transform together with the detection of low vessel density was proposed in [25]. Other methods were based on machine learning using hand-crafted features [5,7,16]. In recent studies, deep CNNs and heuristic based clustering have achieved a high accuracy [6].

Most previous methods focus on specific criteria that are insufficient to represent the OD and the fovea in all images, such as the highest variation in intensity of adjacent pixels [9,11]. Some studies combine several indicators, like the entropy of the image or the convergence of the main vessels, but the way that those indicators are used is very restrictive. This means that the method fails when any of these indicators does not follow the standard pattern [16,25]. In these cases, this indicator must be ignored and other indicators must be considered instead. The proposed method is based on several complementary indicators to represent the areas where both the OD and the fovea are located. However, the hand-crafted parameters of the method are not as restrictive as the previously mentioned methods. In addition, the combination of the proposed saliency maps provides complementary information. Hence, the detection is successful even for

the specific cases where the OD and the fovea do not show a standard appearance. As a consequence, the proposed method shows a high generalization ability. Deep learning approaches also have some limitations, being the lack of transparency and interpretability the most critical [26]. Previous methods for the OD and fovea detection based on deep learning frameworks are end-to-end solutions where many hyperparameter settings are involved [6,27]. The optimization of these hyperparameters is a complex and critical task [6]. Moreover, the clinical indicators defining the OD and fovea locations, such as the relative position of the vasculature, are not easily related to the internal operations performed by the network. For this reason, it is difficult to debug the method when the deep network fails, which hinders the quality control. Additionally, deep learning methods require large amounts of data to perform effectively and are significantly more complex than the traditional methods [26]. In contrast, the proposed method is based on various saliency maps whose interpretability is direct. Further, a high generalization ability is achieved using only a few images to estimate most parameters.

Firstly, we applied a preprocessing stage to normalize the inter-image and intra-image appearance and enhance retinal structures. Then, we obtained an estimation of the retinal background. Subsequently, the vasculature was segmented. Finally, we introduced novel methods to locate the OD and fovea centers. For these tasks, we performed a direct combination of various complementary saliency maps computed over the image. To obtain these maps, we considered the spatial relationships between the main anatomical structures of the retina as well as their visual features. To the best of our knowledge, this is the first time that the maps proposed in this work have been extracted from fundus images. Another contribution of this work is the proposed retinal background extraction algorithm, applied over the preprocessed image. This algorithm is based on the detection of the dark and bright pixels [28] and is complemented by two novel steps: a binarization operation and a region-growing technique.

2. MATERIALS

We used a proprietary database and three public databases: DiaretDB1 [29], DRIVE [30] and Messidor [31]. The method was developed using a set of images from the proprietary dataset (training set). The public databases allowed us to assess the robustness of the proposed method.

2.1 Proprietary database

The proprietary dataset consisted of 564 retinal images provided by the "Instituto Universitario de Oftalmobiología Aplicada" (IOBA) of the University of Valladolid (Valladolid, Spain) and the "Hospital Clínico Universitario de Valladolid" (Valladolid, Spain). All subjects gave their informed consent to participate in the study. Our research was conducted in accordance with the Declaration of Helsinki, and the protocol was approved by the Ethics Committee at "Hospital Clínico Universitario de Valladolid". Images were captured using a Topcon TRC-NW400 retinal camera at a 45-degree Field of View (FOV) and stored in 24-bit JPEG format. All images had a resolution of 1956 × 1934 pixels. Two images were captured per eye: one fovea-centered and one OD-centered. An ophthalmologist manually annotated the OD and fovea centers in all the images in this database. The database was randomly divided into two balanced sets: training set (281 images) and test set (283 images).

2.2 DiaretDB1

The DiaretDB1 [29] database is composed of 89 images captured in the Kuopio University Hospital. They were captured at a 50-degree FOV and have a resolution of 1500 × 1552 pixels. All the images were fovea-centered.

2.3 DRIVE

The DRIVE [30] dataset consists of 40 images obtained from a diabetic screening program conducted in the Netherlands. The size of the images was 565 × 584 pixels, stored in 24-bit TIFF format. All the images were fovea-centered. In our experiments for the detection of the fovea, 3 images were excluded for not showing a visually detectable fovea [8].

2.4 Messidor

The Messidor [31] database comprises 1200 images captured using a Topcon TRC NW6 retinal camera at a 45-degree FOV. They were stored in 24-bit TIFF format at three different resolutions: 1440 × 960, 2240 × 1488 and 2304 × 1536 pixels. All the images were fovea-centered.

3. METHODS

3.1 Overview

The proposed method comprises several stages. For an overview of the method, Figure 1 is provided. The image I_{prep} is the result of the preprocessing stage. Three images were obtained

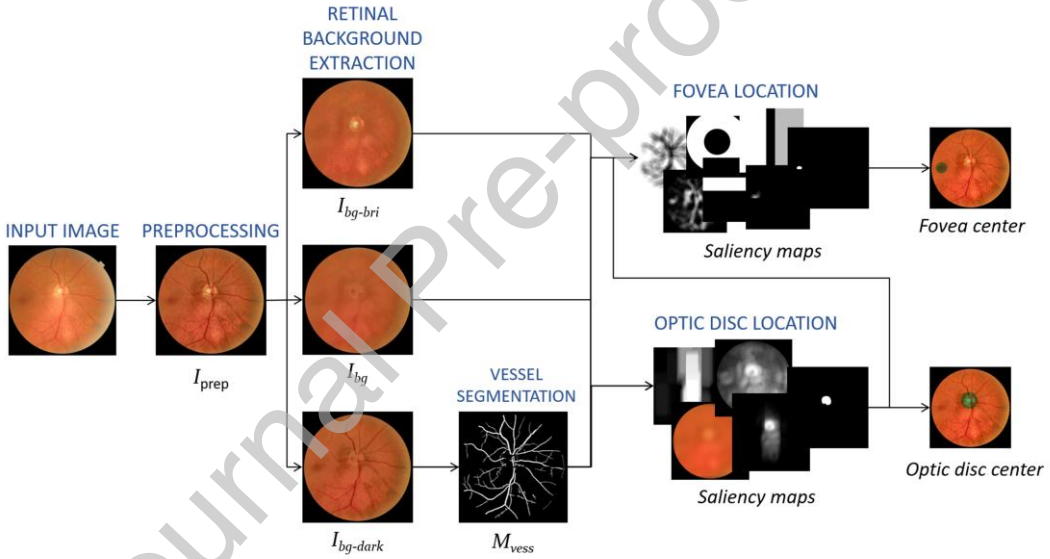

Figure 1. Overview of the proposed method. The image I_{prep} is the result of the preprocessing stage. I_{bg} is the estimated background of the fundus image after removing both bright and dark structures. I_{bg-bri} is the estimated background after removing the dark structures while preserving the bright ones. $I_{bg-dark}$ is the estimated background after removing the bright structures while preserving the dark ones. The image M_{vess} corresponds to the vessel segmentation result from $I_{bg-dark}$. For the subsequent detection of the OD and the fovea, various saliency maps were computed using the previous obtained images. Finally, the saliency maps were combined to obtain the final centers.

from the retinal background extraction: I_{bg} is the estimated background of the fundus image after removing both bright and dark structures; I_{bg-bri} is the estimated background after removing the dark structures while preserving the bright ones; and $I_{bg-dark}$ is the estimated background after removing the bright structures while preserving the dark ones. The image M_{vess} corresponds to the vessel segmentation result from $I_{bg-dark}$. For the subsequent detection of the OD and the fovea, various saliency maps were computed using the previous obtained images. Finally, the saliency maps were combined to obtain the final centers. All these stages are detailed in the following subsections.

3.2 Preprocessing

Retinal fundus images frequently show both local and overall nonuniform illumination, poor contrast and noise [32,33]. Moreover, the intrinsic features of the patient also affect image appearance [34,35]. These drawbacks make it hard to detect the anatomical structures of the eye. Therefore, a preprocessing stage is required. In this study, we applied our method in [28]. It

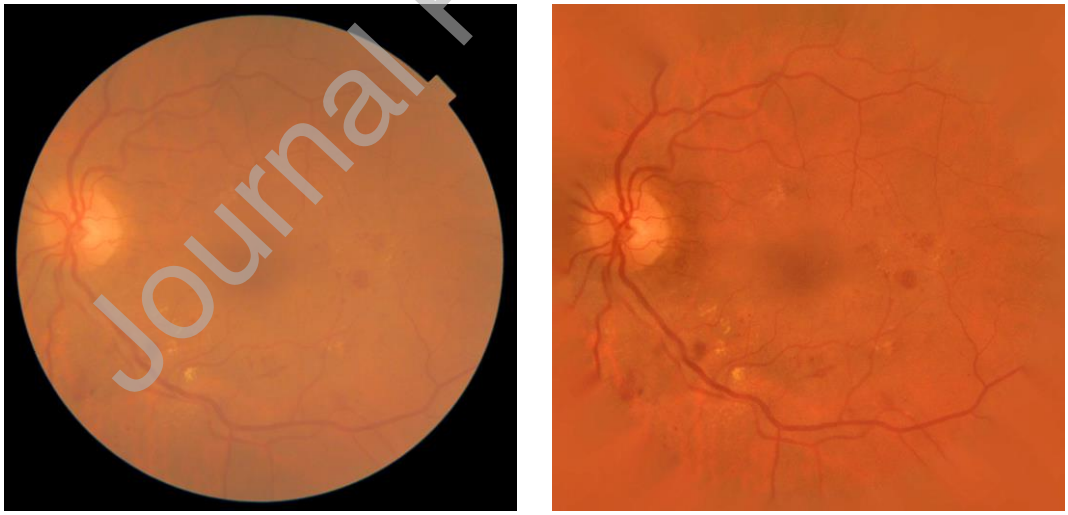

(a) (b)

Figure 2. Preprocessing stage. (a) Original image. (b) Preprocessed image, I_{prep}, after applying bright border artifact removal, background extension, illumination and color equalization, denoising and contrast enhancement.

is composed of five sequential operations: bright border artifact removal, background extension, illumination and color equalization, denoising and contrast enhancement. With this method, we highlighted the retinal landmarks, while achieving intra-image and inter-image normalization. The result of this stage, I_{prep}, can be seen in Fig. 2. In addition, this stage allowed us to obtain de diameter of the FOV, *D*, which is used in subsequent steps.

3.3 Background extraction

Fundus images can be modeled as the combination of a background, corresponding to the retinal tissue, and a foreground, which covers the retinal structures and the visible lesions [36]. This foreground can be divided into dark and bright pixels. In this stage, the aim was to estimate the background of the fundus image, I_{bg}, as if it was free of any vascular structures or visible lesions. At the same time, we intended to obtain a version of I_{prep} lacking dark pixels, named I_{bg-bri}, and a version of I_{prep} lacking bright pixels, named $I_{bg-dark}$.

For this task, we first detected the dark pixels in I_{prep} (I_{dark}), using the multiscale algorithm in [28]. Likewise, we detected the bright pixels in I_{prep} (I_{bri}) by applying an adaption of the same multiscale operation:

$$I_{bri} = \max_{s} \alpha_s \left(\left(I_{prep} + I_{dark} \right) - I_{bg,s} \right). \quad (1)$$

The parameter s represents a scale dependent on *D* (FOV diameter). It was empirically settled to $s = \left\{ \frac{D}{48}, \frac{D}{24}, \frac{D}{12}, \frac{D}{6}, \frac{D}{3} \right\}$ [28]. The parameter $I_{bg,s}$ is the background of I_{dark}, estimated with a mean filter of size s. Finally, the parameter α_s was defined as [28]:

$$\alpha_s = 1 - \left(3.84 \frac{s}{D} \right). \quad (2)$$

The next step was to binarize the high intensity pixels (peak pixels) in the images I_{dark} and I_{bri}. The thresholds were empirically set and guaranteed that all peak pixels were selected:

$$M_{dark} = \begin{cases} 0, & I_{dark} < 0.005 \\ 1, & I_{\text{dark}} \geq 0.005 \end{cases}. \quad (3)$$

$$M_{bri} = \begin{cases} 0, & I_{bri} < 0.01 \\ 1, & I_{\mathrm{bri}} \geq 0.01 \end{cases}. \quad (4)$$

Finally, $I_{bg-dark}$ was calculated. First, we eliminated the pixels in I_{prep} that matched M_{bri}. Then, we filled them by applying a region-growing algorithm. This algorithm iteratively dilated the image r pixels in order to fill the eliminated pixels with new values. To calculate the value for each new filled pixel, we computed the average value of its surrounding pixels in a neighborhood of $w \times w$ pixels. In this work, r was in the range $[\frac{D}{1000}, \frac{D}{8}]$ and w in the range $[\frac{D}{1000}, \frac{D}{4}]$. Both r and w grew by an empirical factor of 1.3 in each iteration. The increase in the value of r allowed us to accelerate the algorithm significantly. The increase of w allowed us to soften the background estimate as the growing region progressed. Dilation was performed iteratively until all the eliminated pixels had been filled, when $I_{bg-dark}$ was obtained.

The image I_{bg-bri} was obtained in a similar way. We eliminated the pixels in I_{prep} that matched M_{dark}. Then, we filled them by applying the region-growing algorithm described above.

Finally, the image I_{bg} was obtained following the same idea. We eliminated the pixels in I_{prep} that matched both M_{dark} and M_{bri}. Then, we filled them by applying the region-growing algorithm previously explained.

All three images obtained in this stage can be seen in Fig. 3. In $I_{bg-dark}$, the bright structures are smoothly removed from I_{prep} while perfectly preserving the dark structures. The image I_{bg-bri} also adequately estimates the retinal background ignoring the dark structures while preserving the bright structures. Image I_{bg} represents the background of the fundus image removing both bright and dark structures.

3.4 Blood vessel segmentation

The orientation and distribution of blood vessels over the retina is useful to detect the OD and the fovea [5]. The aim of this stage was to detect the pixels associated with the vascular network in the fundus image, M_{vess}. For this task, we developed a method based on [37]. We noticed that, using the method in [37] alone, the edges of the exudates and other bright regions were frequently detected as blood vessel segments (Fig. 4b). In order to decrease false detections, we used the image $I_{bg-dark}$ as input image instead of the original fundus image. This allowed us to improve the segmentation notably, as shown in Fig. 4c.

3.5 Optic disc location

The OD location is useful for monitoring glaucoma and detecting neovascularization within it.

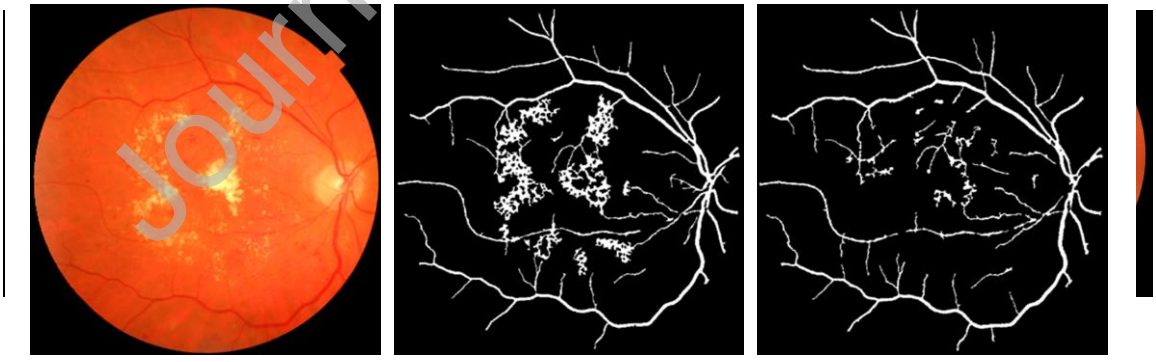

(a) (b) (c)

Figure 4. Blood vessel segmentation stage. (a) Original image. (b) Segmented mask using I_{prep} as input. The edges of the bright lesions are incorrectly detected as blood vessel segments. (c) Segmented mask using $I_{bg-dark}$ as input. The edges of the bright lesions are not detected as part of the vasculature.

Additionally, it is helpful to automatically detect the fovea [5]. Frequently, parts inside the OD can be potentially classified as abnormalities, such as exudates, since their appearance may be very similar [5]. Therefore, the OD location is also useful in algorithms for the detection of some pathologies, such as the DR. In this stage, the OD center was automatically detected. Then, the OD was modeled as a circle whose radius, R_{OD}, was estimated as $\frac{D}{12}$ pixels [17].

The main blood vessels pass through the OD almost vertically. It means that the OD is always around the area where more vertical vessels are found [38]. To select this area, we first applied a morphological opening over the binary image M_{vess} using a linear morphological operator with

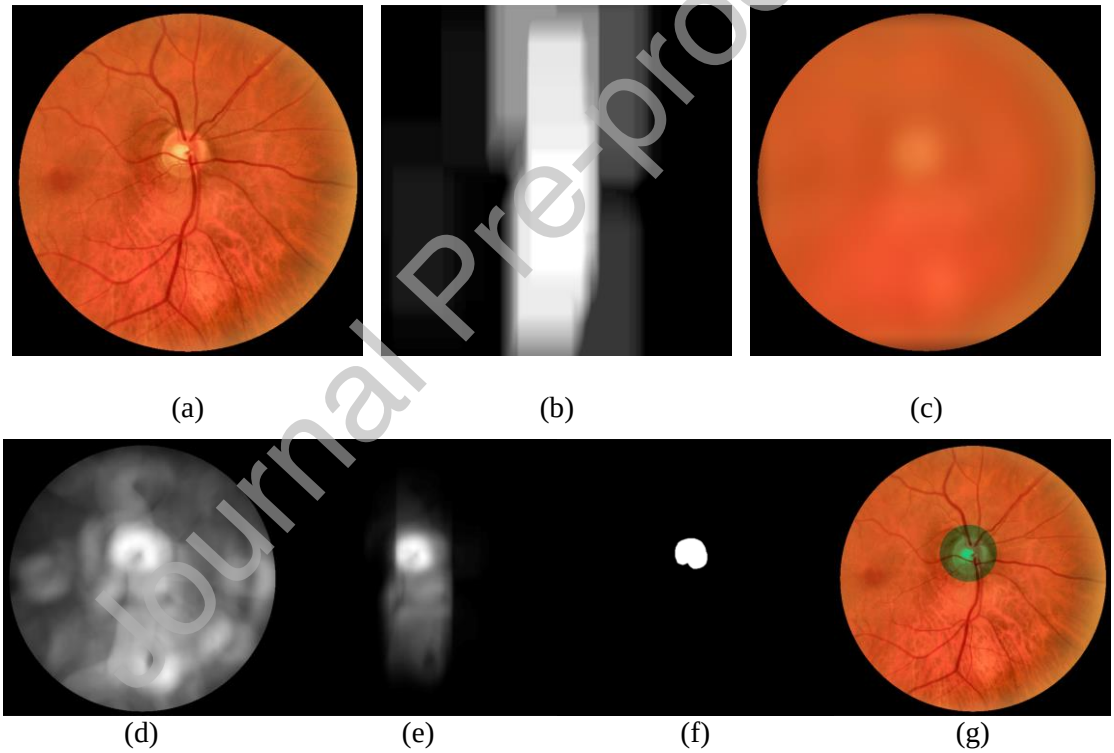

Figure 5. Saliency maps for the detection of the OD. (a) Preprocessed image I_{prep}. (b) Image I_{vvr}, representing the area around the vertical blood vessels. (c) Image $I_{corr-OD}$, representing the correlation between the image I_{bg-bri} and a circle. (d) Image I_{std}, the local standard deviation over the red channel of I_{prep}. (e) Image I_{OD} as a combination of the previous saliency maps. (f) Brightest pixels in I_{OD}. (g) Centroid of the region I_{OD}: final location of the OD. The complete OD was approximated by a circle.

vertical orientation and size empirically set to $\frac{D}{50}$ pixels to detect the main segments of the vertical vessels. Then, we applied a rectangular shaped spatial filter. The size of this filter was empirically determined, with a width of R_{OD} and a height of $4 * R_{OD}$ pixels, which ensures that the main arcades are covered. This allowed us to cover the whole area where the OD potentially is, obtaining the image I_{vvr} (Fig. 5b). The next step was based on template matching. We computed the correlation between the image I_{bg-bri} and a circle with radius R_{OD} used as template, obtaining the color image $I_{corr-OD}$ (Fig. 5c). Additionally, the red channel of I_{prep} frequently showed a high local standard deviation where the OD was located. Therefore, we also applied a local standard deviation filter using a disk element with radius R_{OD} over the red channel of I_{prep} to obtain the image I_{std} (Fig. 5d). This radius was empirically chosen to cover the area of the OD.

In order to combine the results of the previous steps, we built a probability map using:

$$I_{OD} = I_{vvr} \cdot I^{G}_{corr-OD} \cdot I^{B}_{corr-OD} \cdot I_{std}, \qquad (5)$$

where the symbol "·" represents the element-wise multiplication. The parameters $I^{G}_{corr-OD}$ and $I^{B}_{corr-OD}$ correspond to the green and blue channels of the image $I_{corr-OD}$, respectively (Fig. 5e).

Finally, we selected the 1% of pixels in I_{OD} with the highest value (see Fig. 5f). This percentage was empirically obtained. In most cases, these pixels formed a single connected component. However, when more than one connected component was detected, we selected the biggest one. The centroid of that region was considered the center of the OD (Fig. 5g).

3.6 Fovea location

Lesions near the fovea are especially relevant [5]. Additionally, since the appearance of the fovea is dark with respect to the background, the detection of red lesions (RLs) can be problematic. Therefore, fovea location is useful for pathology detection algorithms and severity graduation. In this stage, the center of the fovea was automatically detected. The macular area, whose center is the fovea, is characterized by the absence of blood vessels. First, we started

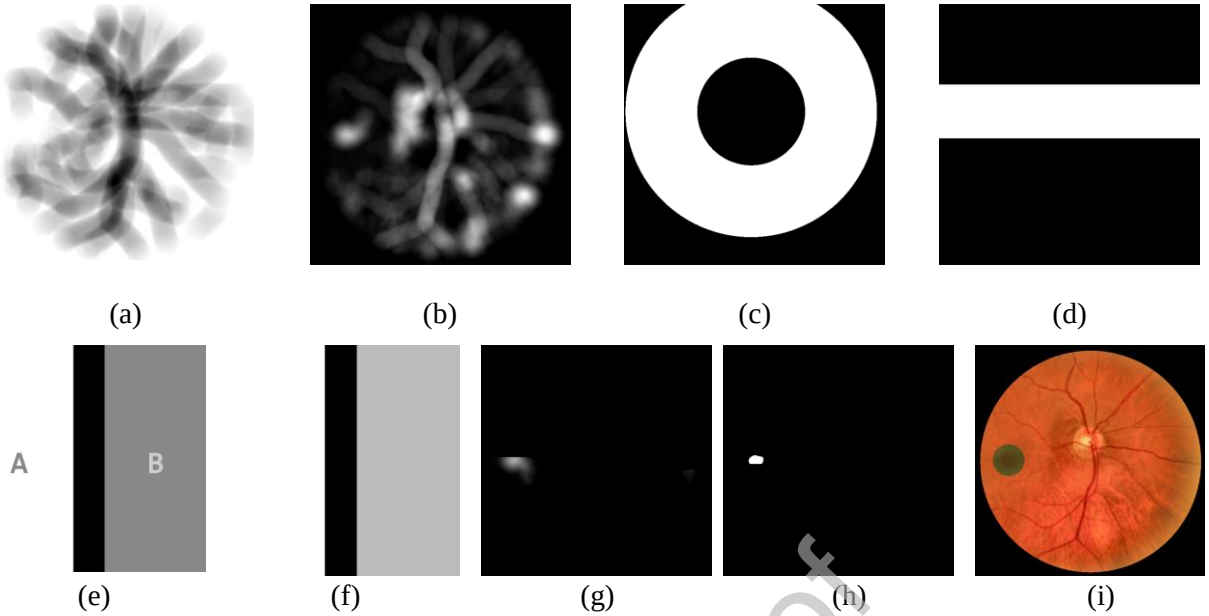

Figure 6. Saliency maps for the detection of the fovea. (a) Image I_{vn}, where the white pixels represent the avascular areas. (b) Image I_{corr-f}, the correlation of $(I_{bg} - I_{bg-dark})$ with a disk. (c) Image M_{ring}, representing a ring centered at the OD center. (d) Image M_{band}, representing a horizontal band vertically aligned with the OD center. (e) Image I_{den-1}, blood vessel density within M_{band}. (f) Image I_{den-2}, blood vessel density outside M_{band}. (g) Image I_{FOVEA}, combination of the previous saliency maps. (h) Brightest pixels in I_{FOVEA}. (i) Centroid of the region I_{FOVEA}: final location of the fovea. The complete fovea was approximated by a circle.

dilating the mask M_{vess} using a disk with small radius of $\frac{R_{OD}}{50}$ pixels to make it slightly thicker. The value of the radius was not crucial. Second, we applied a disk-shaped spatial filter with a radius of $\frac{2}{3}R_{OD}$ pixels. This value allows covering the vicinity of the vasculature without reaching the fovea. Third, the complement of the processed image was computed. These operations allowed us to obtain the image I_{vn}, which represents the avascular areas of the image (Fig. 6a).

The next step was based on template matching. Since the fovea is located at the center of a darker area, we first subtracted the images I_{bg} and $I_{bg-dark}$ to get the dark pixels in $I_{bg-dark}$. Second, we calculated the correlation between the image resulting from this subtraction and a

disk with radius $\frac{R_{OD}}{2}$, used as the template. Hence, we considered that the radius of the fovea is approximately half the radius of the OD. Then, we obtained the image I_{corr-f} as the maximum, computed pixel by pixel, of the red and green channels of the correlation image (Fig. 6b). Next, we considered the fact that the fovea is always located at an approximately constant distance from the OD. After analyzing the training dataset, we noticed that the fovea is always located between three and seven times R_{OD} from the OD. Therefore, we built a ring centered at the OD center, with the minor radius $3R_{OD}$ pixels and the major radius $7R_{OD}$ pixels. This mask was M_{ring} (Fig. 6c). Then, we considered that the fovea is always approximately located at the same vertical level as the OD in the fundus image. Accordingly, we built another mask, M_{band}, covering a horizontal band with $3R_{OD}$ pixels high and vertically aligned with the center of the OD (Fig. 6d). This estimated height was set by analyzing the training dataset. The next step of the fovea location method required dividing the image into two regions, R=$\{A, B\}$, with a vertical line passing through the center of the OD (Fig. 6e). This step allowed us to detect the temporal side (where the fovea is), based on the density of blood vessels. For each part, we assigned all of its pixels the value of the blood vessel density within M_{band}, computed as:

$$VD_{in-band_R} = \frac{M_{vess} \times M_{in-band_R}}{Area_R}, \qquad R = \{A, B\}, \tag{6}$$

being $M_{in-band_R}$ the pixels of M_{band} in the region R and $Area_R$ the area of the region R. In this way, we obtained the image I_{den-1} (Fig. 6e). We then computed the blood vessel density outside M_{band} as:

$$VD_{out-band_R} = \frac{M_{vess} \times M_{out-band_R}}{Area_R}, \qquad R = \{A, B\}, \tag{7}$$

being $M_{out-band_R}$ the pixels outside M_{band} in the region R. For each part of the divided image (A/B), we assigned all of its pixels the value $VD_{out-band_R}$. Thus, the image I_{den-2} was obtained (Fig. 6f).

Finally, all of the previous complementary information was combined as:

$$I_{FOVEA} = I_{vn} \cdot I_{corr-f} \cdot M_{ring} \cdot M_{band} \cdot I_{den-1} \cdot I_{den-2}, \quad (8)$$

where the symbol "·" refers to the element-wise multiplication. The image I_{FOVEA} can be seen as a probability map (see Fig. 6g). We selected the 0.2% of the pixels in I_{FOVEA} with the highest value (see Fig. 6h). This percentage was empirically obtained. In most cases, those pixels formed a single connected component. However, when more than one connected component was detected, we selected the biggest one. The centroid of that region was considered the center of the fovea (see Fig. 6i).

4. RESULTS

The methods for the OD and fovea location were evaluated over the test set of the proprietary dataset (283 images) and the public databases DiaretDB1 (89 images), DRIVE (40 images) and Messidor (1200 images). The accuracy was computed comparing the automatically detected center with the center annotated by the ophthalmologist as:

$$Acc = \frac{C}{N}, \quad (9)$$

where *C* is the number of correct detections and *N* is the total number of tested images. We considered a correct detection when the Euclidean distance between both points (distance error) was lower than a certain threshold (DE_{max}). Otherwise, the detection was considered incorrect. As in other studies for both OD and fovea location, we considered $DE_{max} = R_{OD}$ pixels [5,17,39]. This way, we can establish a direct comparison with the rest of the methods in literature. The results of the proposed methods for the OD and fovea location are shown in Table 1.

Table 1. Results for the location of the optic disc and the fovea.

Database	Number of test images	Optic disc location accuracy	Fovea location accuracy
Proprietary	283	100%	100%
DiaretDB1	89	100%	100%
DRIVE	40*	100%	100%
Messidor	1200	99.5%	99.67%

*3 images did not show the fovea and were discarded for the fovea detection method [8,29]

Additionally, we calculated the overlapping area between the ground truth and the estimated OD. Given that the edges of the fovea are undefined, this measure was not calculated for the detected fovea. Since the ophthalmologist only provided us with the ground truth center, both the ground truth and the estimated OD were modeled as a circle with radius $\frac{D}{12}$ pixels [17]. Then, we computed the overlapping ratio between both circles as [14,40–42]:

$$S = \frac{Area(T \cap D)}{Area(T \cup D)}, \quad (10)$$

where T is the ground truth circle and D is the estimated OD circle obtained using the proposed method. For all the images in test set of the proprietary database, the average overlapping ratio was 0.826.

5. DISCUSSION AND CONCLUSIONS

In this study, we proposed automatic methods for OD and fovea location. The initial preprocessing stage was useful for inter-image and intra-image normalization, achieving consistent outputs for the operations applied on every image. The method for the retinal background extraction is an important contribution in this study. The brightest and darkest pixels were replaced with the estimated retinal background, obtaining a realistic result. This

method could also be valuable in further studies related to fundus image processing. Using this method, we improved the vascular network segmentation, preventing the edges of the EXs and other bright regions from being wrongly detected as blood vessel segments. The methods to locate the OD and the fovea formed the main stages of the proposed algorithm. We introduced novel saliency maps based on the spatial relationships between the main anatomical structures of the retina and their characteristic visual appearance. These maps provided a great generalization ability.

The proposed methods for the OD and fovea location were assessed using four retinal image databases. The test set of the proprietary database was used to validate the overall performance. The public databases DiaretDB1, DRIVE and Messidor allowed us to evaluate the robustness and generalization ability of the proposed method. It should be noted that all the images included in the databases used in this study were obtained based on a specific capture protocol. According to this protocol, all images contained the vasculature, the OD and the fovea within the FOV. Only 3 images from the DRIVE database did not show a visible fovea and were discarded for the fovea detection method. In addition, both the OD and the fovea were in the expected region of the OD (EROD) defined in [43]. However, some of the images had poor quality. Therefore, these images could not meet the rules of autodetection [43]. Nonetheless, no image was discarded due to low quality. It is also important to mention that all the parameters of the method are defined as a fraction of *D*. Therefore, they are relative to the FOV size and the method is independent to the image resolution.

The results for the OD location method showed 100% accuracy for all databases, except for Messidor. In this database we achieved 99.5% accuracy, which means that only 6 detections out of 1200 images were incorrect. These results are in line with those in other studies, as shown in Table 2. The results for the DRIVE database are the same as in other studies (100% accuracy). As for DiaretDB1, only two previous studies reported 100% accuracy [20,44]. Our method

Table 2. Results for the automatic location of the optic disc.

Study	DRIVE	DiaretDB1	Messidor
Sinthanayothin et al. 1999 [11]	60.00	-	-
Walter et al. 2002 [12]	80.00	-	-
Welfer et al. 2010 [47]	100	97.50	-
Aquino et al. 2010 [48]	-	-	99.00
Lu and Lim 2011 [49]	97.50	98.88	-
Lu 2011 [15]	-	-	98.77
Hsiao et al. 2012 [17]	100	-	-
Qureshi et al. 2012 [16]	100	97.79	-
Yu et al. 2012 [50]	-	-	99.00
Pereira et al. 2013 [18]	100	93.25	-
Giachetti et al. 2013 [25]	-	-	99.67
Basit and Fraz 2015 [51]	100	98.88	-
Yu et al. 2015 [45]	100	99.88	99.67
Harangi et al. 2015 [7]	100	98.88	98.33
Rahebi and Hardalaç 2016 [19]	100	94.38	-
Sa'ed Abed et al. 2016 [20]	100	100	-
Abdullah et al. 2016 [44]	100	100	99.25
Diaz-Pernil et al. 2016 [52]	97.50	97.75	-
Alshayeji et al. 2017 [53]	100	97.75	-
Chalakkal et al. 2018 [14]	100	97.70	98.60
Al-Bander et al. 2018 [6]	-	-	97.00
Proposed method	**100**	**100**	**99.50**

outperforms the location accuracy obtained in all the previous methods for the Messidor database, except for Guiachetti et al. [25] and Yu et al. [45]. However, no results were provided for DRIVE and DiaretDB1 databases in [25]. Meanwhile, the method proposed in [45] obtained a lower accuracy than our method for the DiaretDB1 database (99.88%).

The average overlapping ratio for all the images in test set of the proprietary database was 0.826. This value is in line with the results obtained by other authors in previous works for different databases, as shown in Table 3. However, this measure is not crucial for our study since the OD boundary was not exhaustively detected. Instead, only the OD center was estimated and the OD boundary was modeled as a circle.

It should be noted that our method failed to locate the OD in certain images. In Fig. 7a there is a bright structure located near the OD area whose shape and size are easily confused with the OD. In Fig. 7b we have a very blurred image. Finally, in Fig. 7c we have a deformed OD, which extends over a large area. However, our method succeeded in locating the OD in other complicated cases. In Fig.8a-e the OD lacks the brightness characteristic. In Fig. 8f-i four poor quality images are shown, where the edge of the OD was not well defined and some vessels were uncertain. Our method also worked well with choroidal and retinal thickness showing a

Table 3. Comparison of average overlapping ratio with previous methods

Database	Method	Average overlapping ratio
DRIVE	Lupascu et ál. 2008 [42]	0.403
	Salazar-Gonzalez et al. 2011[41]	0.707
	Morales et al. 2013 [40]	0.716
	Chalakkal et ál. 2018 [14]	0.868
DiaretDB1	Lupascu et ál. 2008 [42]	0.309
	Salazar-Gonzalez et al. 2011 [41]	0.757
	Morales et al. 2013 [40]	0.817
	Chalakkal et ál. 2018 [14]	0.821
Messidor	Yu et ál. 2011 [54]	0.830
	Omid et ál. 2015 [55]	0.860
	Chalakkal et ál. 2018 [14]	0.880
Proprietary database	**Proposed method**	**0.826**

large bright peripapillary region (see Fig. 8f-g) or images presenting prominent exudates (see Fig. 8h).

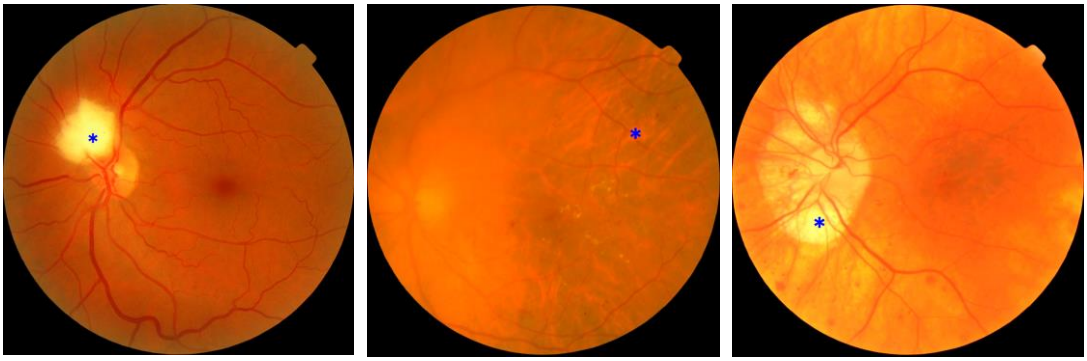

(a) (b) (c)

Figure 7. Examples where the OD is incorrectly detected. (a) Image with a bright structure located near the true OD. (b) Very blurred image. (c) Image with choroidal and retinal thickness showing a large bright peripapillary region.

The results for the fovea location method also showed 100% accuracy for all databases, except for Messidor (99.66%). These results are in line with those in other studies, as shown in Table 4. We excluded three images that did not present visually detectable fovea in DRIVE database, as in [8]. All the foveas in the remaining 37 images were correctly detected (100% accuracy). The same accuracy was obtained by GeethaRamani and Balasubramanian [46] but using only 35 out of 40 images. The accuracy obtained by Qureshi et al. [16] was lower using the DRIVE database (91.73%). As for the DiaretDB1 database, to the best of our knowledge, our method obtained the highest accuracy in the literature, correctly locating the foveas in all DiaretDB1 images. Considering the Messidor database, our method also outperformed the accuracy of previous studies. It should be noted that, although the fovea location was based on the previous OD location, less false fovea detections than false OD detections were obtained. This is because some false OD detections were not far from the actual center annotated by the ophthalmologist, as shown in Fig. 9.

Regarding the fovea location, some false detections were also obtained. The poor quality in Fig. 10a and the irregular background in Fig. 10b make the fovea unclear. In Fig. 10c we have the

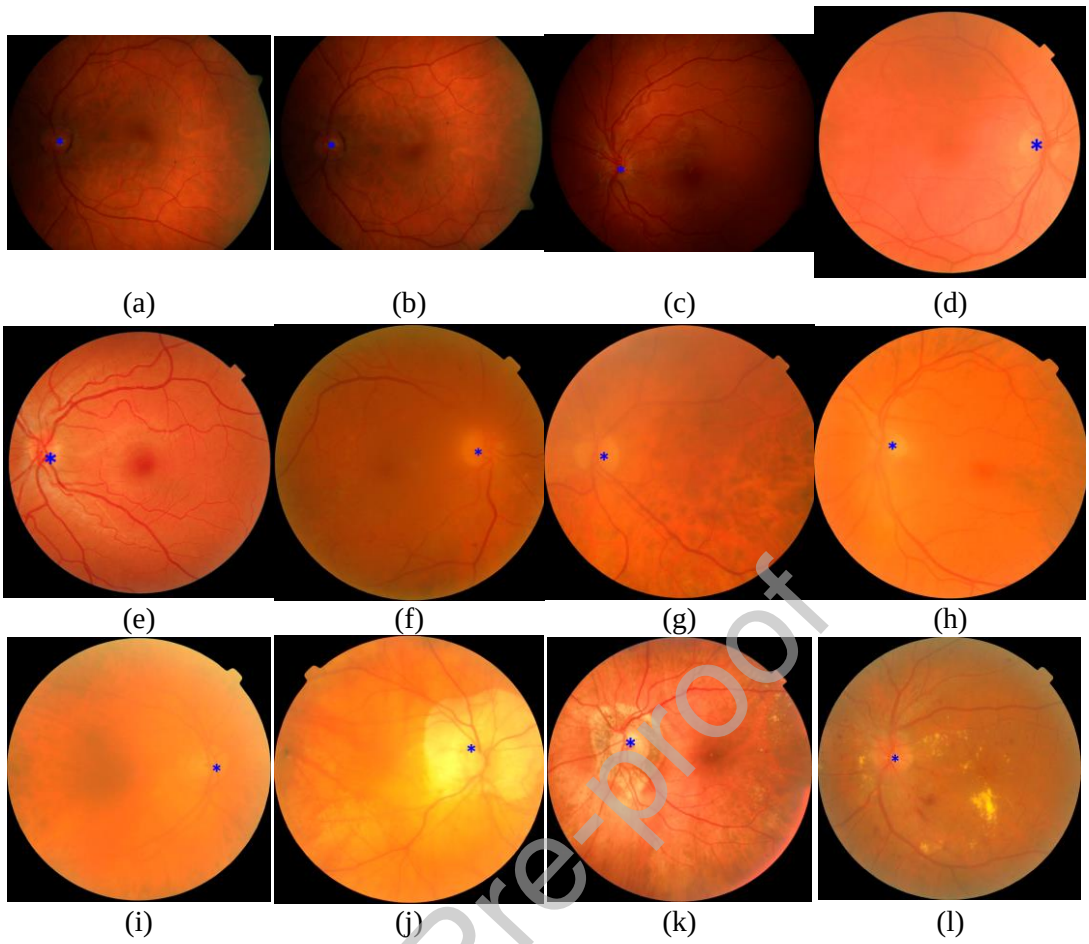

Figure 8. Examples where the OD is successfully detected. (a-e) Images where the OD lacks the brightness characteristic. (f-i) Poor quality images, where the edge of the OD is not well defined and some vessels are uncertain. (j-k) Images with choroidal and retinal thickness, showing a large bright peripapillary region. (l) Image having prominent exudates.

same example as in Fig. 8b. Since the OD detection was far from the ground truth, the subsequent fovea detection was incorrect. However, our method succeeded in detecting the fovea center in several complicated examples. In Fig. 11a-b, correct detections over poor quality images are shown. In Fig. 11c-d, large dark areas hide the fovea boundaries. Finally, in Fig. 11e-h we can see that our method properly locates the fovea even in the presence of different types of lesions.

When it comes to the algorithmic and computational complexities of our approach, the proposed saliency maps are computed by combining a small number of spatial filters with morphological

operations and basic algebra. Therefore, the algorithmic implementation is straightforward. For the computation, we used Matlab® on a computer having Intel Core i7-7770 CPU @ 3.60GHz and 32GB RAM. The average computational time of the proposed algorithms using DRIVE, DiaretDB1 and Messidor databases is shown in Table 5. In this study, we have employed the

Table 4. Results for the automatic location of the fovea.

Study	DRIVE	DiaretDB1	Messidor
Welfer et al. 2011 [8]	100	92.13	-
Qureshi et al. 2012 [16]	91.73	98.74	-
Gegundez-Arias et al. 2013 [21]	-	-	96.92
Giachetti et al. 2013 [25]	-	-	99.10
Aquino 2014 [22]	-	94.38	98.24
GeethaRamani and Balasubramanian 2018 [46]	100	97.75	99.33
Al-Bander et al. 2018 [6]	-	-	96.60
Proposed method	**100**	**100**	**99.67**

images at full resolution. As observed for the tested databases, the image resolution exponentially affects the computation time. For this reason, a direct computational time comparison of the methods must be made with caution. However, for any of the considered resolutions, the proposed method provides sufficient speed for high workloads in automatic eye

(a) (b)

Figure 9. Images where the OD is incorrectly detected. However, since the OD detection is close to the real center, the automatic detection of the fovea is correct.

screening [25].

(a) (b) (c)

Figure 10. Examples where the fovea is incorrectly detected. (a) Poor quality image. (b) Image with irregular background. (c) Image where the fovea detection is incorrect because of the previous incorrect detection of the OD (see Fig. 6b).

The proposed method has some limitations that should be mentioned. First, it has been developed assuming the presence of both the OD and the fovea within the FOV, giving an estimation of the centers even if any of the landmarks were not present. In addition, the OD and

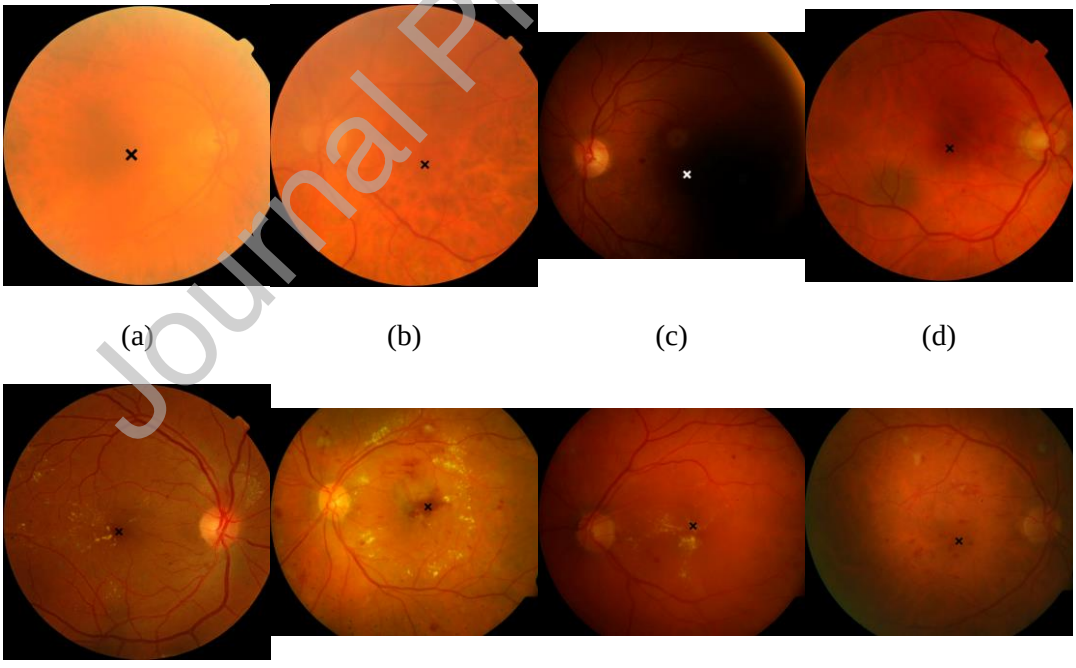

(a) (b) (c) (d)

(e) (f) (g) (h)

Figure 11. Examples where the fovea is successfully detected. (a-b) Poor quality images. (c-d) Images where the fovea boundaries are hidden by large dark areas. (e-h) Images showing different types of lesions.

Table 5. Average computational time per image of the proposed algorithms.

Method	DRIVE 565×584	DiaretDB1 1500×1552	Messidor 1440×960, 2240×1488, 2304×1536
Optic disc location	0.42 s.	12.22 s.	23.29 s.
Fovea location	0.12 s.	2.33 s.	3.75 s.

the fovea must be approximately located at the same vertical level in the fundus image. If a different capture protocol is considered, the proposed method would have to be adapted. Second, the method for the automatic fovea location relies on the previous OD detection. Although a close OD estimation is sufficient, we intend to detect the fovea independently from the OD in future studies. Third, the blood vessel segmentation is required for the OD detection. However, a rough segmentation is sufficient. Moreover, the background extraction method proposed in this study allowed us to prevent false blood vessel detections. In future studies, we will try to eliminate the vasculature detection stage. The method was developed using 281 images and tested using 1612 images from four different databases. Despite the great variability, we will try to increase the number of fundus images in future studies. Having a large database, we could take advantage of deep learning techniques to optimize the salience maps as a complement to the proposed method. Thereby, we will verify whether this technology helps to improve the results.

In conclusion, our methods have proved effective and robust. The novel algorithm for the retinal background extraction is valuable for fundus image processing and the proposed saliency maps showed a great generalization ability. Since the OD and fovea locations are crucial for the detection of multiple diseases, such as glaucoma, age-related macular degeneration (AMD) and DR, the proposed method could be useful in different CADS.

ACKNOWLEDGEMENTS

This research was supported by 'Ministerio de Ciencia, Innovación y Universidades' and 'European Regional Development Fund' (FEDER) under projects DPI2017-84280-R and PGC2018-098214-A-I00, by 'European Commission' and FEDER under projects 'Análisis y correlación entre el genoma completo y la actividad cerebral para la ayuda en el diagnóstico de la enfermedad de Alzheimer' and 'Análisis y correlación entre la epigenética y la actividad cerebral para evaluar el riesgo de migraña crónica y episódica en mujeres' ('Cooperation Programme Interreg V-A Spain-Portugal POCTEP 2014–2020'), and by 'CIBER de Bioingeniería, Biomateriales y Nanomedicina (CIBER-BBN)' through 'Instituto de Salud Carlos III' co-funded with FEDER funds. Roberto Romero-Oraá has a predoctoral scholarship from the 'Junta de Castilla y León' and European Social Fund. Javier Oraá-Pérez has a 'Ayudas para la contratación de personal técnico de apoyo a la investigación' grant from the 'Junta de Castilla y León' funded by the European Social Fund and Youth Employment Initiative.

CONFLICT OF INTEREST

There are no conflicts of interest that could inappropriately influence this research work.

ETHICAL APPROVAL

This study was approved by the Ethics Committee of the "Hospital Clínico Universitario de Valladolid", Valladolid, Spain.

AUTHORSHIP RESPONSIBILITY

- The material in this manuscript is original and contains no matter libelous or otherwise unlawful.

- The manuscript represents valid work and that neither this manuscript nor any other with substantially similar content under my authorship has been published or is being considered for publication elsewhere.

- I have participated sufficiently in the work to take public responsibility for all its content.

REFERENCES

[1] N.H. Cho, J.E. Shaw, S. Karuranga, Y. Huang, J.D. da Rocha Fernandes, A.W. Ohlrogge, B. Malanda, IDF Diabetes Atlas: Global estimates of diabetes prevalence for 2017 and projections for 2045, Diabetes Res. Clin. Pract. (2018). https://doi.org/10.1016/j.diabres.2018.02.023.

[2] M.D. Abramoff, M.K. Garvin, M. Sonka, Retinal imaging and image analysis, IEEE Rev. Biomed. Eng. 3 (2010) 169–208. https://doi.org/10.1109/RBME.2010.2084567.

[3] H.F. Jelinek, M.J. Cree, Automated image detection of retinal pathology, 2009. https://doi.org/10.1201/9781420037005.

[4] M. Niemeijer, M.D. Abràmoff, B. van Ginneken, Image structure clustering for image quality verification of color retina images in diabetic retinopathy screening, Med. Image Anal. 10 (2006) 888–898. https://doi.org/10.1016/j.media.2006.09.006.

[5] M. Niemeijer, M.D. Abràmoff, B. van Ginneken, Fast detection of the optic disc and fovea in color fundus photographs, Med. Image Anal. 13 (2009) 859–870. https://doi.org/10.1016/j.media.2009.08.003.

[6] B. Al-Bander, W. Al-Nuaimy, B.M. Williams, Y. Zheng, Multiscale sequential convolutional neural networks for simultaneous detection of fovea and optic disc, Biomed. Signal Process. Control. 40 (2018) 91–101. https://doi.org/10.1016/j.bspc.2017.09.008.

[7] B. Harangi, A. Hajdu, Detection of the optic disc in fundus images by combining probability models, Comput. Biol. Med. 65 (2015) 10–24. https://doi.org/10.1016/j.compbiomed.2015.07.002.

[8] D. Welfer, J. Scharcanski, D.R. Marinho, Fovea center detection based on the retina anatomy and mathematical morphology, Comput. Methods Programs Biomed. 104 (2011) 397–409. https://doi.org/10.1016/j.cmpb.2010.07.006.

[9] M. Lalonde, M. Beaulieu, L. Gagnon, Fast and robust optic disc detection using pyramidal decomposition and hausdorff-based template matching, IEEE Trans. Med. Imaging. 20 (2001) 1193–1200. https://doi.org/10.1109/42.963823.

[10] M. García, C.I. Sánchez, M.I. López, D. Abásolo, R. Hornero, Neural network based detection of hard exudates in retinal images, Comput. Methods Programs Biomed. 93 (2009) 9–19. https://doi.org/10.1016/j.cmpb.2008.07.006.

[11] C. Sinthanayothin, J.F. Boyce, H.L. Cook, T.H. Williamson, Automated localisation of the optic disc, fovea, and retinal blood vessels from digital colour fundus images, Br. J. Ophthalmol. 83 (1999) 902–910. https://doi.org/10.1136/bjo.83.8.902.

[12] T. Walter, J.-C. Klein, P. Massin, A. Erginay, A contribution of image processing to the diagnosis of diabetic retinopathy--detection of exudates in color fundus images of the human retina., IEEE Trans. Med. Imaging. 21 (2002) 1236–1243. https://doi.org/10.1109/TMI.2002.806290.

[13] A. Hoover, M. Goldbaum, Locating the optic nerve in a retinal image using the fuzzy convergence of the blood vessels, IEEE Trans. Med. Imaging. 22 (2003) 951–958. https://doi.org/10.1109/TMI.2003.815900.

[14] R.J. Chalakkal, W.H. Abdulla, S.S. Thulaseedharan, Automatic detection and segmentation of optic disc and fovea in retinal images, IET Image Process. 12 (2018) 2100–2110. https://doi.org/10.1049/iet-ipr.2018.5666.

[15] S. Lu, Accurate and efficient optic disc detection and segmentation by a circular

transformation, IEEE Trans. Med. Imaging. 30 (2011) 2126–2133. https://doi.org/10.1109/TMI.2011.2164261.

[16] R.J. Qureshi, L. Kovacs, B. Harangi, B. Nagy, T. Peto, A. Hajdu, Combining algorithms for automatic detection of optic disc and macula in fundus images, Comput. Vis. Image Underst. 116 (2012) 138–145. https://doi.org/10.1016/j.cviu.2011.09.001.

[17] H.K. Hsiao, C.C. Liu, C.Y. Yu, S.W. Kuo, S.S. Yu, A novel optic disc detection scheme on retinal images, Expert Syst. Appl. 39 (2012) 10600–10606. https://doi.org/10.1016/j.eswa.2012.02.157.

[18] C. Pereira, L. Gonçalves, M. Ferreira, Optic disc detection in color fundus images using ant colony optimization, Med. Biol. Eng. Comput. 51 (2013) 295–303. https://doi.org/10.1007/s11517-012-0994-5.

[19] J. Rahebi, F. Hardalaç, A new approach to optic disc detection in human retinal images using the firefly algorithm, Med. Biol. Eng. Comput. 54 (2016) 453–461. https://doi.org/10.1007/s11517-015-1330-7.

[20] S. Abed, S.A. Al-Roomi, M. Al-Shayeji, Effective optic disc detection method based on swarm intelligence techniques and novel pre-processing steps, Appl. Soft Comput. J. 49 (2016) 146–163. https://doi.org/10.1016/j.asoc.2016.08.015.

[21] M.E. Gegundez-Arias, D. Marin, J.M. Bravo, A. Suero, Locating the fovea center position in digital fundus images using thresholding and feature extraction techniques, Comput. Med. Imaging Graph. 37 (2013) 386–393. https://doi.org/10.1016/j.compmedimag.2013.06.002.

[22] A. Aquino, Establishing the macular grading grid by means of fovea centre detection using anatomical-based and visual-based features, Comput. Biol. Med.

55 (2014) 61–73. https://doi.org/10.1016/j.compbiomed.2014.10.007.

[23] H. Li, O. Chutatape, Automated Feature Extraction in Color Retinal Images by a Model Based Approach, IEEE Trans. Biomed. Eng. 51 (2004) 246–254. https://doi.org/10.1109/TBME.2003.820400.

[24] M. Niemeijer, M.D. Abràmoff, B. Van Ginneken, Segmentation of the optic disc, macula and vascular arch in fundus photographs, IEEE Trans. Med. Imaging. 26 (2007) 116–127. https://doi.org/10.1109/TMI.2006.885336.

[25] A. Giachetti, L. Ballerini, E. Trucco, P.J. Wilson, The use of radial symmetry to localize retinal landmarks, Comput. Med. Imaging Graph. 37 (2013) 369–376. https://doi.org/10.1016/j.compmedimag.2013.06.005.

[26] P. Mamoshina, A. Vieira, E. Putin, A. Zhavoronkov, Applications of Deep Learning in Biomedicine, Mol. Pharm. 13 (2016) 1445–1454. https://doi.org/10.1021/acs.molpharmaceut.5b00982.

[27] Y. Jiang, L. Duan, J. Cheng, Z. Gu, H. Xia, H. Fu, C. Li, J. Liu, JointRCNN: A Region-Based Convolutional Neural Network for Optic Disc and Cup Segmentation, IEEE Trans. Biomed. Eng. 67 (2020) 335–343. https://doi.org/10.1109/TBME.2019.2913211.

[28] R. Romero-Oraá, J. Jiménez-García, M. García, M.I. López-Gálvez, J. Oraá-Pérez, R. Hornero, Entropy rate superpixel classification for automatic red lesion detection in fundus images, Entropy. 21 (2019). https://doi.org/10.3390/e21040417.

[29] T. Kauppi, V. Kalesnykiene, J.-K. Kamarainen, L. Lensu, I. Sorri, A. Raninen, R. Voutilainen, H. Uusitalo, H. Kalviainen, J. Pietila, DIARETDB1 diabetic retinopathy database and evaluation protocol, in: Procedings Br. Mach. Vis.

Conf. 2007, 2007. https://doi.org/10.5244/C.21.15.

[30] J. Staal, M.D. Abràmoff, M. Niemeijer, M.A. Viergever, B. Van Ginneken, Ridge-based vessel segmentation in color images of the retina, IEEE Trans. Med. Imaging. 23 (2004) 501–509. https://doi.org/10.1109/TMI.2004.825627.

[31] E. Decencière, X. Zhang, G. Cazuguel, B. Laÿ, B. Cochener, C. Trone, P. Gain, J.R. Ordóñez-Varela, P. Massin, A. Erginay, B. Charton, J.C. Klein, Feedback on a publicly distributed image database: The Messidor database, Image Anal. Stereol. 33 (2014) 231–234. https://doi.org/10.5566/ias.1155.

[32] L. Seoud, T. Hurtut, J. Chelbi, F. Cheriet, J.M.P. Langlois, Red Lesion Detection Using Dynamic Shape Features for Diabetic Retinopathy Screening, IEEE Trans. Med. Imaging. 35 (2016) 1116–1126. https://doi.org/10.1109/TMI.2015.2509785.

[33] B. Wu, W. Zhu, F. Shi, S. Zhu, X. Chen, Automatic detection of microaneurysms in retinal fundus images, Comput. Med. Imaging Graph. 55 (2017) 106–112. https://doi.org/10.1016/j.compmedimag.2016.08.001.

[34] C.I. Sánchez, M. García, A. Mayo, M.I. López, R. Hornero, Retinal image analysis based on mixture models to detect hard exudates, Med. Image Anal. 13 (2009) 650–658. https://doi.org/10.1016/j.media.2009.05.005.

[35] S.H. Rasta, M.E. Partovi, H. Seyedarabi, A. Javadzadeh, A comparative study on preprocessing techniques in diabetic retinopathy retinal images: illumination correction and contrast enhancement, J. Med. Signals Sens. 5 (2015) 40–8. http://www.ncbi.nlm.nih.gov/pubmed/25709940 (accessed January 31, 2019).

[36] M. Foracchia, E. Grisan, A. Ruggeri, Luminosity and contrast normalization in retinal images, Med. Image Anal. 9 (2005) 179–190.

https://doi.org/10.1016/j.media.2004.07.001.

[37] A.M. Mendonça, S. Member, A. Campilho, Segmentation of Retinal Blood Vessels by Combining the Detection of Centerlines and Morphological Reconstruction, 25 (2006) 1200–1213.

[38] C.I. Sanchez, R. Hornero, M.I. López, M. Aboy, J. Poza, D. Abásolo, C.I. Sánchez, R. Hornero, M.I. López, M. Aboy, J. Poza, D. Abásolo, A novel automatic image processing algorithm for detection of hard exudates based on retinal image analysis., Med. Eng. Phys. 30 (2008) 350–7. https://doi.org/10.1016/j.medengphy.2007.04.010.

[39] J.P. Medhi, S. Dandapat, Automatic detection of fovea using property of vessel free region, 2015 21st Natl. Conf. Commun. NCC 2015. (2015). https://doi.org/10.1109/NCC.2015.7084852.

[40] S. Morales, V. Naranjo, U. Angulo, M. Alcaniz, Automatic detection of optic disc based on PCA and mathematical morphology, IEEE Trans. Med. Imaging. 32 (2013) 786–796. https://doi.org/10.1109/TMI.2013.2238244.

[41] A.G. Salazar-Gonzalez, Y. Li, X. Liu, Optic disc segmentation by incorporating blood vessel compensation, in: IEEE SSCI 2011 - Symp. Ser. Comput. Intell. - CIMI 2011 2011 IEEE 3rd Int. Work. Comput. Intell. Med. Imaging, 2011: pp. 1–8. https://doi.org/10.1109/CIMI.2011.5952040.

[42] C.A. Lupaşcu, L. Di Rosa, D. Tegolo, Automated detection of optic disc location in retinal images, in: Proc. - IEEE Symp. Comput. Med. Syst., 2008: pp. 17–22. https://doi.org/10.1109/CBMS.2008.15.

[43] U. Sevik, C. Köse, T. Berber, H. Erdöl, Identification of suitable fundus images using automated quality assessment methods, J. Biomed. Opt. 19 (2014) 046006.

https://doi.org/10.1117/1.jbo.19.4.046006.

[44] M. Abdullah, M.M. Fraz, S.A. Barman, Localization and segmentation of optic disc in retinal images using circular Hough transform and grow-cut algorithm, PeerJ. 2016 (2016) e2003. https://doi.org/10.7717/peerj.2003.

[45] T. Yu, Y. Ma, W. Li, Automatic localization and segmentation of optic disc in fundus image using morphology and level set, in: Int. Symp. Med. Inf. Commun. Technol. ISMICT, IEEE Computer Society, 2015: pp. 195–199. https://doi.org/10.1109/ISMICT.2015.7107527.

[46] R. GeethaRamani, L. Balasubramanian, Macula segmentation and fovea localization employing image processing and heuristic based clustering for automated retinal screening, Comput. Methods Programs Biomed. 160 (2018) 153–163. https://doi.org/10.1016/j.cmpb.2018.03.020.

[47] D. Welfer, J. Scharcanski, C.M. Kitamura, M.M. Dal Pizzol, L.W.B. Ludwig, D.R. Marinho, Segmentation of the optic disk in color eye fundus images using an adaptive morphological approach, Comput. Biol. Med. 40 (2010) 124–137. https://doi.org/10.1016/j.compbiomed.2009.11.009.

[48] A. Aquino, M.E. Gegúndez-Arias, D. Marín, Detecting the optic disc boundary in digital fundus images using morphological, edge detection, and feature extraction techniques, IEEE Trans. Med. Imaging. 29 (2010) 1860–1869. https://doi.org/10.1109/TMI.2010.2053042.

[49] S. Lu, J.H. Lim, Automatic optic disc detection from retinal images by a line operator, IEEE Trans. Biomed. Eng. 58 (2011) 88–94. https://doi.org/10.1109/TBME.2010.2086455.

[50] H. Yu, E.S. Barriga, C. Agurto, S. Echegaray, M.S. Pattichis, W. Bauman, P.

Soliz, Fast localization and segmentation of optic disk in retinal images using directional matched filtering and level sets, IEEE Trans. Inf. Technol. Biomed. 16 (2012) 644–657. https://doi.org/10.1109/TITB.2012.2198668.

[51] A. Basit, M.M. Fraz, Optic disc detection and boundary extraction in retinal images., Appl. Opt. 54 (2015) 3440–7. https://doi.org/10.1364/AO.54.003440.

[52] D. Díaz-Pernil, I. Fondón, F. Peña-Cantillana, M.A. Gutiérrez-Naranjo, Fully automatized parallel segmentation of the optic disc in retinal fundus images, Pattern Recognit. Lett. 83 (2016) 99–107. https://doi.org/10.1016/j.patrec.2016.04.025.

[53] M. Alshayeji, S.A. Al-Roomi, S. Abed, Optic disc detection in retinal fundus images using gravitational law-based edge detection, Med. Biol. Eng. Comput. 55 (2017) 935–948. https://doi.org/10.1007/s11517-016-1563-0.

[54] H. Yu, S. Barriga, C. Agurto, S. Echegaray, M. Pattichis, G. Zamora, W. Bauman, P. Soliz, Fast localization of optic disc and fovea in retinal images for eye disease screening, in: R.M. Summers, B. van Ginneken (Eds.), Med. Imaging 2011 Comput. Diagnosis, SPIE, 2011: p. 796317. https://doi.org/10.1117/12.878145.

[55] S. Omid, J. Shanbehzadeh, Z. Ghassabi, S.S. Ostadzadeh, Optic disc detection in high-resolution retinal fundus images by region growing, in: Proc. - 2015 8th Int. Conf. Biomed. Eng. Informatics, BMEI 2015, Institute of Electrical and Electronics Engineers Inc., 2016: pp. 101–105. https://doi.org/10.1109/BMEI.2015.7401481.